Chemical Engineering Journal 523 (2025) 168741

Contents lists available at ScienceDirect

Chemical Engineering Journal

journal homepage: www.elsevier.com/locate/cej

Molecular motion–structure–property correlation in a polymorphic AIEgen with mechanochromic and piezoelectric functions

Kaiwei Huang [a], Tao Jiang [a], Jiexi Liang [a], Xiaoxue Chen [a], Wei Liu [a], Wenxuan Cai [a], Chongyang Zeng [a], Junru Chen [a,*], Jun Zhang [c,*], Changyong (Chase) Cao [b,*], Xing Feng [a,*]

[a] Guangdong Provincial Key Laboratory of Functional Soft Condensed Matter, School of Materials and Energy, Guangdong University of Technology, Guangzhou, 510006, PR China
[b] Laboratory for soft Machines and Electronics, Department of Mechanical and Aerospace Engineering, Case Western Reserve University, Cleveland, OH, 44106, USA
[c] School of Materials and Chemical Engineering, Anhui Jianzhu University, Hefei, 230601, PR China

ARTICLE INFO

Keywords:
Aggregation-induced emission (AIE)
Excitation-dependent emission
Mechanofluorochromism
Piezoelectric properties
Motion–structure–property relationship

ABSTRACT

Establishing direct correlations between molecular motion, crystal structure, and macroscopic properties is essential for designing responsive functional materials. Herein, we report a malononitrile-based aggregation-induced emission luminogen (AIEgen), **TPA-CN**, that crystallizes into multiple polymorphs exhibiting distinct optoelectronic behaviors. In dilute solution, **TPA-CN** exhibits excitation-dependent emission spanning from sky blue to red under irradiation from 375 to 425 nm, arising from conformational flexibility and multiple excited-state transitions. In the solid state, subtle differences in crystal packing—governed by torsional angles and intermolecular interactions that modulate dipole moments—lead to pronounced variations in luminescence color and piezoelectric response. Mechanical grinding induces mechanochromic emission shifts without phase transitions, as confirmed by powder X-ray diffraction (PXRD). Comparative analysis of crystallographic data, Hirshfeld surface mapping, and non-covalent interaction (NCI) calculations reveals that weak intermolecular interactions critically regulate crystal packing, ultimately producing distinct emission colors and behaviors. Notably, the non-centrosymmetric polymorph ($Pca2_1$) exhibits strain-sensitive piezoelectric currents up to 562 pA under 0.51 % strain, with a piezoelectric coefficient (d_{33}) of 1.77 pm·V^{-1} and a low Young's modulus of 6.75 GPa. Parallel device configurations further enhance mechanical sensitivity, enabling detection of micro-vibrations. This study reveals how minor conformational changes, and polymorphic packing can orchestrate dual photonic and piezoelectric functions, establishing a unified motion–structure–property paradigm. These insights advance the rational design of multifunctional organic materials for flexible sensing, soft electronics, and energy-harvesting applications.

1. Introduction

Molecules are the fundamental building blocks of matter, and their structures directly govern their physical and chemical properties. Rather than existing in isolation, molecules spontaneously assemble into aggregates through a combination of inter- and intra-molecular interactions, such as van der Waals forces, hydrogen bonding, and electrostatic attractions and molecular motions [1,2]. This aggregation typically lowers the system's energy, stabilizing it and leading to emergent macroscopic properties. Among these phenomena, aggregation-induced emission (AIE) is particularly noteworthy. AIE luminogen (AIEgen) exhibits non-emissive behavior in dilute solution but becomes highly emissive upon aggregation [3,4]. This behavior is primarily attributed to the restriction of intramolecular motion (RIM), which suppresses non-radiative decay pathways and enhances radiative transitions in the aggregated state.

External stimuli—such as temperature, pressure, light, and electric fields—profoundly influence molecular aggregation and endow materials with tunable properties [5–7]. Mechanochromic materials, for instance, respond to mechanical forces by changing color [8,9], which has been applied to advanced applications in security writing and piezo patterning, [9] anti-counterfeit, [10] and temperature detection, [11] as well as electrical energy harvesting, [12] etc. On a molecular level, this behavior arises from conformational rearrangements and changes in

* Corresponding authors.
E-mail addresses: comecjr@gdut.edu.cn (J. Chen), zhangjun@ahjzu.edu.cn (J. Zhang), ccao@case.edu (C.(C. Cao), hyxhn@sina.com (X. Feng).

https://doi.org/10.1016/j.cej.2025.168741
Received 14 July 2025; Received in revised form 13 September 2025; Accepted 19 September 2025
Available online 24 September 2025
1385-8947/© 2025 The Authors. Published by Elsevier B.V. This is an open access article under the CC BY-NC-ND license (http://creativecommons.org/licenses/by-nc-nd/4.0/).

intermolecular interactions, often accompanied by crystal packing transitions or amorphization [13,14]. Yet, a precise understanding of how mechanical forces modulate these molecular motions—and how such dynamics correlate with macroscopic optical changes—remains elusive.

Tang and coworkers previously demonstrated that AIE crystals could undergo elastic deformation and reversible luminescence changes due to RIM and external mechanical perturbations [15]. These findings highlight the potential of AIE crystals as platforms for investigating the intricate relationships between molecular motion, structure, and function. Simultaneously, non-centrosymmetric crystals are known to exhibit piezoelectricity—a coupling between mechanical deformation and electrical polarization [16]. This direct piezoelectric effect enables their application in flexible electronics, sensors, and energy harvesters [17–19]. Organic piezoelectric materials are especially attractive due to their molecular tunability and mechanical compliance [12]. For example, a Co(II)-based coordination cage has shown a piezoelectric coefficient (d_{33}) of 2.8 pC/N [20], while π-π-stacked pyrene-based crystals have demonstrated d_{33} values as high as 8.02 ± 0.26 pm/V [21]. However, materials with very high d_{33} values (e.g., $PbTiO_3$) are often brittle [22], limiting their utility in flexible systems. Thus, optimizing the trade-off between piezoelectric performance and mechanical flexibility remains a key challenge in organic materials. Additionally, crystalline luminescent materials that exhibit mechanochromism often undergo phase transitions upon grinding or pressing, but the deeper coupling between molecular-scale motion, crystal packing alterations, and property evolution is still poorly understood [23–25].

Tetraphenylethylene (TPE) is a prominent AIEgen and has served as the foundation for numerous novel derivatives [26,27]. However, its inherently weak electron-donating ability often results in TPE-decorated derivatives exhibiting poorly defined donor-acceptor (D-A) structure, thereby limiting effective intramolecular charge transfer (ICT). By contrast, the triphenylamine (TPA) unit is a stronger electron donor, featuring a central nitrogen atom connected to three phenyl rings in a 3D propeller-like geometry with C_3 symmetry, making it an excellent building block for constructing AIEgens [28,29]. Inspired by the classic TPE-based AIEgen, we designed "TPE-like" based D-A molecules incorporating the TPA unit for multifunctional applications. In this study, we developed a pull-push architecture based on malononitrile, yielding a red-emissive luminogen (**TPA-CN**) with aggregation-induced emission enhancement (AIEE) characteristics. This system enables investigation of how molecular conformation and crystal packing across diverse space groups dictate photophysical properties. In **TPA-CN**, the 2-(diphenylmethylene)malononitrile group [30] acts as a strong electron acceptor, while the TPA unit functions as the electron donor, together facilitating efficient ICT. The resulting crystals provide a platform to study how minute variations in packing affect macroscopic behaviors such as color change and piezoelectric response. **TPA-CN** exhibits excitation-dependent emission in solution due to intramolecular freedom, while in the solid state, its mechanochromic behavior arises not from phase transitions but from molecular motion-induced packing alterations. Crystals with higher symmetry ($Pca2_1$, $C2v$) show red emission, while those with lower symmetry ($P2_12_12_1$, $D2$) emit orange-red. Moreover, the piezoelectric current generated by the non-centrosymmetric crystal increases with strain, reaching 562 pA at 0.51 % strain. The material's low Young's modulus (6.75 GPa) and moderate d_{33} (1.77 pm V^{-1}) highlight its potential for flexible sensing applications, including ground vibration detection.

2. Materials and methods

2.1. Chemicals and measurement

Unless otherwise stated, all reagents were purchased from commercial sources and were used without further purification. Tetrahydrofuran (THF) was distilled before use. ^1H and ^{13}C NMR spectra were recorded on a Bruker AVANCE III 400 M spectrometer using $CDCl_3$ as the solvent ($CHCl_3$, ^1H: d = 7.26 ppm, ^{13}C: d = 77.06 ppm). Coupling constant (J) values are given in hertz (Hz). High-resolution mass spectra (HRMS) were recorded using an LC/MS/MS, which consisted of a High-Performance Liquid Chromatography (HPLC) system (Ultimate 3000 RSLC, Thermo Scientific, USA) and a Q Exactive Orbitrap mass spectrometer. UV–Vis absorption spectra and photoluminescence spectra were recorded on a Shimadzu UV-2600 and a Hitachi F-4700 fluorescence spectrometer. Photoluminescence quantum yields were measured using an absolute method on a Hamamatsu Quantaurus-QY spectrometer (C11347–11) equipped with a 3.3-inch integrating sphere.

The quantum lifetimes were recorded on an Edinburgh FLS 980 instrument and measured using a time-correlated single-photon counting method. Cyclic voltammetry (CV) experiments were performed in acetonitrile (ACN) containing 0.1 M tetrabutylammonium hexafluorophosphate ($n\text{-}Bu_4NPF_6$) as the supporting electrolyte. A standard three-electrode configuration was employed, consisting of a glassy carbon disk working electrode, a platinum wire counter electrode, and an Ag/AgCl reference electrode. The ferrocene/ferrocenium (Fc/Fc^+) redox couple was used as an internal reference. CV scans were initiated at 0 V, swept forward to +1.6 V, and then reversed to 0 V at a scan rate of 100 mV/s under ambient conditions. Quantum chemistry calculations were conducted at both the ground state and aggregated state using the Gaussian 09 W software package with the B3LYP functional and 6-31G basis set. Powder XRD patterns were recorded on a Bruker D8 ADVANCE X-ray diffractometer, using Cu K_α radiation (λ = 1.54 Å, 40 mA, 40 mV).

2.2. Synthesis and characterization

(4-(diphenylamino)phenyl)(phenyl)methanone (2): Under a nitrogen atmosphere, mixture of 4-bromobenzophenone (300 mg, 1.15 mmol, 1.0 eq.), diphenylamine (233 mg,1.38 mmol, 1.2 eq.), K_2CO_3 (2.5 g, 14.49 mmol, 16 eq.) and P(t-Bu)$_3$ (2.32 g, 11.49 mmol, 10 eq.) in toluene (10 mL) solution was stirred 10 min at room temperature, Pd(OAc)$_2$ (103 mg, 0.46 mmol) were added. Then, the mixture was stirred and heated to 100 °C for 24 h. After it was cooled, the mixture was quenched by H_2O (50 mL) and extracted by dichloromethane (CH_2Cl_2) (50 mL × 3) three times; the combined organic layer was successively washed with water and brine (50 mL) and dried over $MgSO_4$ and evaporated. The residue was purified by column chromatography eluting with hexane to give **2** as a yellow solid (295 mg, 74 %). ^1H NMR (400 MHz, $CDCl_3$) δ 7.78 (d, J = 7.6 Hz, 2H), 7.72 (d, J = 8.8 Hz, 2H), 7.55 (t, J = 7.4 Hz, 1H), 7.46 (t, J = 7.5 Hz, 2H), 7.33 (t, J = 7.9 Hz, 4H), 7.19 (d, J = 6.8 Hz, 4H), 7.14 (t, J = 7.3 Hz, 2H), 7.02 (d, J = 8.7 Hz, 2H) ppm. ^{13}C NMR (100 MHz, $CDCl_3$) δ 195.2, 152.0, 146.5, 138.5, 132.0, 131.7, 129.7, 129.6, 128.2, 126.0, 124.7, 119.6 ppm.

2-((4-(diphenylamino)phenyl)(phenyl)methylene)malononitrile (TPA-CN): Under a nitrogen atmosphere, mixture of intermediate **2** (295 mg, 0.85 mmol, 1.0 eq.) and malononitrile (558 mg, 8.45 mmol, 10 eq.) in pyridine (10 mL) solution was stirred and heated to 110 °C for 48 h. After it was cooled, the pyridine was disposed of under reduced pressure. The residue was purified by column chromatography eluting with CH_2Cl_2 to give **TPA-CN** as a red solid (147 mg, 44 %). ^1H NMR (400 MHz, $CDCl_3$) δ 7.55 (t, J = 7.2 Hz, 1H), 7.47 (t, J = 7.6 Hz, 2H), 7.42 (d, J = 6.8 Hz, 2H), 7.38–7.30 (m, 6H), 7.19 (d, J = 7.1 Hz, 6H), 6.92 (d, J = 9.0 Hz, 2H) ppm. ^{13}C NMR (100 MHz, $CDCl_3$) δ 173.6, 152.4, 145.6, 136.7, 132.7, 132.0, 130.5, 129.8, 128.7, 126.6, 125.6, 118.3, 115.2, 114.9 ppm. HRMS (ESI) m/z: calcd. For $C_{28}H_{19}N_3$ $[M + H]^+$: 398.1652; found, 398.1653.

2.3. X-ray crystallography

Crystallographic data for **TPA-CN** based **Crystal I**, **Crystal III** and **Crystal IV** were collected on a Bruker APEX 2 CCD diffractometer with graphite monochromated Mo Kα radiation (λ = 0.71073 Å) in the ω scan mode or on a Rigaku AFC12 diffractometer equipped with a HyPix

detector and a rotating anode source, also with Mo Kα radiation. [31] The structures were solved by charge flipping or direct methods algorithms and refined by full-matrix least-squares methods on F2. [32,33] Further details are provided in Table S5. The CCDC numbers are 2451778 for **Crystal I**, 2451780 for **Crystal III** and 2451779 for **Crystal IV**, respectively, which contain the supplementary crystallographic data for this paper. These data can be obtained free of charge from The Cambridge Crystallographic Data Centre via www.ccdc.cam.ac.uk/structures.

2.4. Fabrication of devices

A suitable **TPA-CN** crystal (dimensions: 60–100 μm in length, 20–35 μm in width, and 8–15 μm in thickness) (Fig. S19) was selected and mounted on a flexible polyimide film substrate (3 cm length × 1 cm width × 100 μm thickness). Silver paste was applied at both ends of the crystal to form electrodes. The fabricated piezoelectric device was tested under ambient air without encapsulation. To ensure high reproducibility of the electrical signals, more than 10 piezoelectric devices were fabricated. All devices demonstrated nearly identical electrical responses under the same measurement conditions.

2.5. Piezoelectric properties measurement

The piezoelectric device was mounted on a LinMot® BF01–37 linear motor by clamping both ends of the polyimide substrate to the motor stage. Electrical contact was established through a probe connection to the device's copper wires. The motor was programmed to execute periodic reciprocal linear motion, thereby applying controlled strain to the device. The resulting piezoelectric response current was measured and recorded using a Keithley 2636B Source Meter.

2.6. Piezoresponse force microscopy (PFM) measurement

A suitable crystal **TPA-CN** (dimensions: 50–100 μm in length, 20–40 μm in width, and 20–30 μm in thickness) was mounted on a silicon wafer, and silver paste was applied at one end of the crystal to form electrodes under microscopic observation. The devices containing **TPA-CN** crystals were positioned on the Atomic Force Microscope (AFM, Bruker, Dimension Fastscan) sample stage, with conductive copper adhesive connecting the sample stage to the silicon wafer. In PFM mode, the AFM was set to a 3 V driving voltage, and the AFM tip scanned a 5 μm range on the crystal surface. The sample's response in both the vertical and horizontal directions was recorded using the AFM's lock-in amplifier to detect surface topography.

3. Results and discussion

3.1. Synthesis, structural characterization, and photophysical properties

The detailed synthetic route for compound **TPA-CN** is illustrated in **Scheme S1** and the molecular structure **TPA-CN** is displayed in Fig. 1. The target molecule was synthesized through a two-step process involving a Buchwald–Hartwig coupling reaction followed by a Knoevenagel condensation, affording **TPA-CN** in a 44 % yield. The molecular structure was confirmed using a combination of $^{1}H/^{13}C$ NMR spectroscopy, high-resolution mass spectrometry (HRMS), and single-crystal X-ray diffraction (SCXRD). **TPA-CN** demonstrates good solubility in a variety of common solvents, including cyclohexane (Cy), CH_2Cl_2, THF, and dimethyl sulfoxide (DMSO), making it suitable for detailed investigation of its structure–property relationships.

The UV–vis absorption and emission spectra of **TPA-CN** were measured in dilute THF solution (~10^{-5} M). As shown in Fig. 2A, the compound exhibits two main absorption bands: one at 292 nm corresponding to local excited (LE) state transitions, and another at 440 nm attributed to ICT [34]. TD-DFT analysis assigns these transitions to $S_0 \rightarrow S_1$ ($f = 0.4980$) for the ICT band and a combination of $S_0 \rightarrow S_2$ ($f = 0.0218$) and $S_0 \rightarrow S_3$ ($f = 0.1950$) for the LE bands (Table S1).

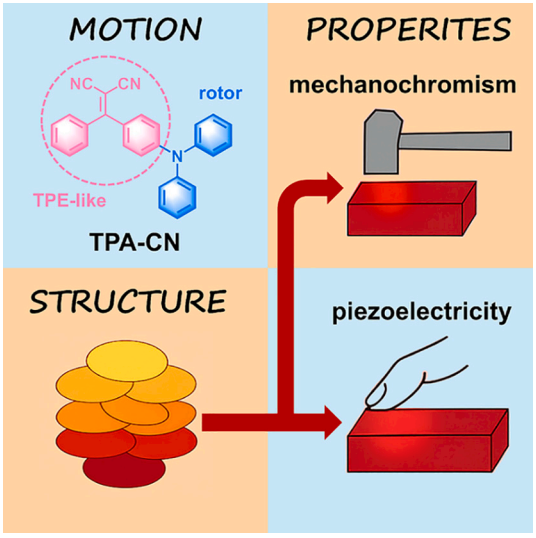

Fig. 1. Schematic illustration of the motion–structure–property relationship in **TPA-CN**-based AIE crystals. Molecular motion of **TPA-CN** influences crystal packing (structure), which governs macroscopic properties including mechanochromism and piezoelectricity. The non-centrosymmetric **Crystal I** (space group *Pca*2$_1$) exhibits both color change under mechanical stimuli and strain-dependent piezoelectric response, enabling applications in flexible sensing devices.

Upon excitation at 375 nm, **TPA-CN** exhibits a weak dual-emission profile with a dominant peak at 480 nm and a shoulder around 616 nm. Notably, as the excitation wavelength is gradually red-shifted from 375 to 425 nm, the emission intensity at 480 nm decreases while the shoulder peak at 617 nm becomes more prominent. This results in a wide-range, color-tunable emission, transitioning from sky-blue to white and finally to red (Fig. 2B). This tunable photoluminescence is further evidenced by the corresponding Commission Internationale de l'Eclairage (CIE) coordinates, which shift from (0.22, 0.27) to (0.33, 0.32), and eventually to (0.55, 0.42), spanning three primary color regions. A strong linear correlation between excitation wavelength and CIE coordinates is observed ($R^2 = 0.9997$) (Fig. 2C), highlighting the excitation-wavelength-dependent emission behavior of **TPA-CN**. This phenomenon likely originates from multiple emissive states inherent to a single molecular structure, consistent with the excited-state conformational diversity [35].

Furthermore, the solvatochromic effect of **TPA-CN** was investigated in six solvents with varying polarities: Cy, toluene, 1,4-dioxane, ethyl acetate, THF and CH_2Cl_2. The ICT absorption band exhibits a gradual red-shift from 434 nm in non-polar Cy to 450 nm in polar CH_2Cl_2 (Fig. S6 and Table S3). Correspondingly, the emission maxima shift significantly from 507 nm in Cy to 630 nm in highly polar THF (λ_{ex} = 440 nm), indicating a strong ICT character (Fig. 2D). Notably, **TPA-CN** maintains excitation-wavelength-dependent emission behavior in intermediate polarity solvents such as 1,4-dioxane and CH_2Cl_2 (Fig. S7). However, in highly polar DMSO, the emission is almost entirely quenched, likely due to enhanced non-radiative decay pathways. These results confirm that **TPA-CN** is a typical donor–acceptor system with strong solvatochromism, where the diphenylamine moiety acts as the electron donor and the 2-(diphenylmethylene)malononitrile moiety serves as the electron acceptor. Concentration-dependent emission spectra of **TPA-CN** in THF solution were recorded over concentrations ranging from 1.0×10^{-7} to 1.0×10^{-3} M. Under excitation at λ_{ex} = 420 nm (Fig. S8), the maximum emission peaks exhibited only slight shifts, confirming that the dominant emission originates from charge-transfer (CT) processes rather than excimer formation.

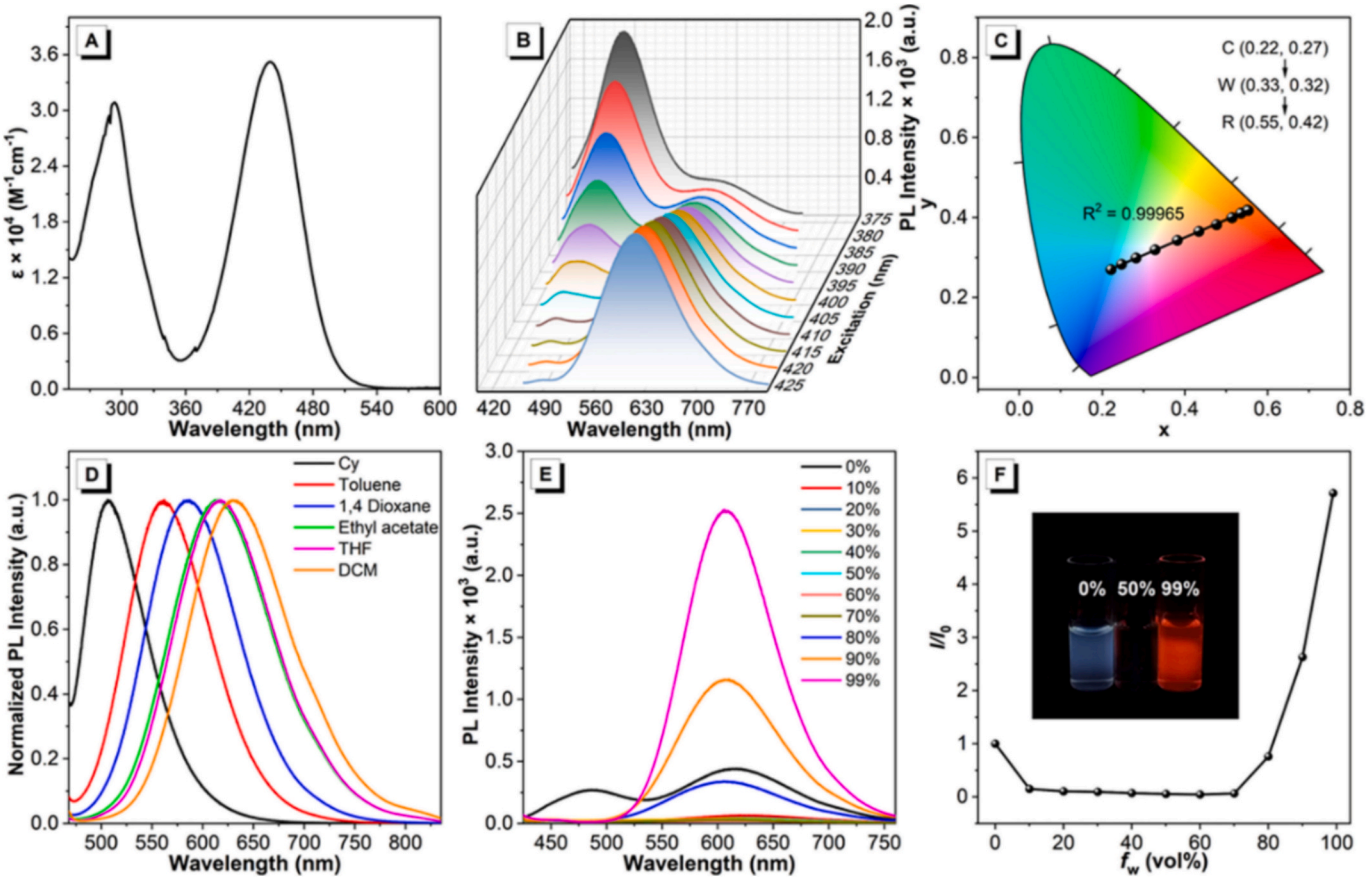

Fig. 2. Photophysical properties of **TPA-CN** in solution and aggregated states. (A) UV–vis absorption spectrum of **TPA-CN** in THF (10^{-5} M), showing characteristic bands attributed to LE and ICT transitions. (B) Excitation wavelength-dependent photoluminescence spectra (λ_{ex} = 375–425 nm), revealing tunable multicolor emission from sky-blue to red. (C) Corresponding CIE chromaticity coordinates, illustrating a linear emission color shift with excitation wavelength (R^2 = 0.9997). (D) Solvent polarity-dependent emission spectra of **TPA-CN** under 440 nm excitation, demonstrating pronounced solvatochromic behavior. (E) Emission spectra in THF/water mixtures with varying water fractions (f_w) at λ_{ex} = 395 nm, exhibiting clear aggregation-induced emission enhancement. (F) Plot of relative emission intensity (I/I_o) versus f_w in THF/water mixtures. Inset: Fluorescence images under 365 nm UV light showing visual emission changes with aggregation.

The AIE characteristics of **TPA-CN** were evaluated in THF/water mixtures with increasing water fractions (f_w). In pure THF (f_w = 0 %), **TPA-CN** exhibits dual emission peaks at 487 and 616 nm under 395 nm excitation, yielding weak cold-white luminescence with a fluorescence quantum yield (Φ_f) below 2.4 %. As f_w increases to 70 %, the short-wavelength emission is gradually quenched, while the long-wavelength emission intensifies, indicative of enhanced ICT upon aggregation. At f_w = 99 %, the emission blue-shifts slightly to 606 nm, accompanied by a > 5.5-fold increase in intensity and a Φ_f of 15.1 % (Table S4). Based on the relationships $k_r = \Phi_f/\tau$ and $k_{nr} = 1/\tau - k_r$, the radiative decay rate (k_r) increases from 5.29×10^6 s^{-1} to 23.4×10^6 s^{-1}, while the non-radiative decay rate (k_{nr}) decreases from 2.15×10^8 s^{-1} to 1.31×10^8 s^{-1}. Thus, compound **TPA-CN** is an AIEE active material. These results confirm a prototypical AIE mechanism: molecular aggregation restricts intramolecular motion, reduces non-radiative decay, and significantly enhances radiative emission. The particle size of TPA-CN at different water fractions (f_w, 0–99 %) was determined by dynamic light scattering (DLS), and the results are presented in Fig. S10. The average aggregate diameters increased from 66.6 nm (f_w = 0 %) to 406.0 nm (f_w = 20 %) and further to 721.9 nm (f_w = 70 %), indicating progressively enhanced aggregation with increasing water content. Interestingly, at f_w = 99 %, where the emission intensity reaches its maximum, the aggregate size was approximately 204.2 nm, which is consistent with previously reported values [36].

3.2. Single crystal X-ray diffraction analysis

TPA-CN was crystallized via slow evaporation from a variety of mixed solvent systems at room temperature to achieve four polymorphs: red rod-shaped **Crystal I** (mixture of hexane and CH_2Cl_2, V_{hexane}:V_{CH2Cl2} = 3:1) and **Crystal II** (mixture hexane and chloroform, V_{hexane}:V_{CHCl3} = 4:1), and orange-red rod-shaped **Crystal III** (in pure CH_2Cl_2) and **Crystal IV** (in pure chloroform solution). High-quality single crystals of **Crystal I, Crystal III,** and **Crystal IV** were characterized using SCXRD (crystallographic parameters in Table S5). **Crystal I** crystallizes in the polar space group $Pca2_1$ (No. 29, C2v) with eight molecules per asymmetric unit, while **Crystals III** and **Crystal IV** adopt the chiral space group $P2_12_12_1$ (No. 19, D2), each with four molecules per asymmetric unit. Although SCXRD analysis of **Crystal II** was unsuccessful due to insufficient crystal quality, its three-dimensional molecular packing was successfully reconstructed using Rietveld refinement of powder X-ray diffraction (PXRD) data. The results indicate that **Crystal II** adopts a triclinic crystal system with space group *P*-1 (Table S9, Figs. S12 and S13).

As shown in Fig. 3A-C and Table 1, all polymorphs exhibit twisted molecular conformations, with torsion angles (θ_1 and θ_2) between the peripheral benzene rings and the central phenyl ring of the TPA unit ranging from 56.72° to 78.79°. Crystals I and II show larger θ_1 values compared to Crystals III and IV, while their θ_2 angles are smaller. In contrast, torsion angles θ_3—associated with the phenyl ring of the 2-(diphenylmethylene)malononitrile acceptor—follow the order: **Crystal II** < **Crystal III** < **Crystal I** < **Crystal IV, and** torsion angles θ_4 follow

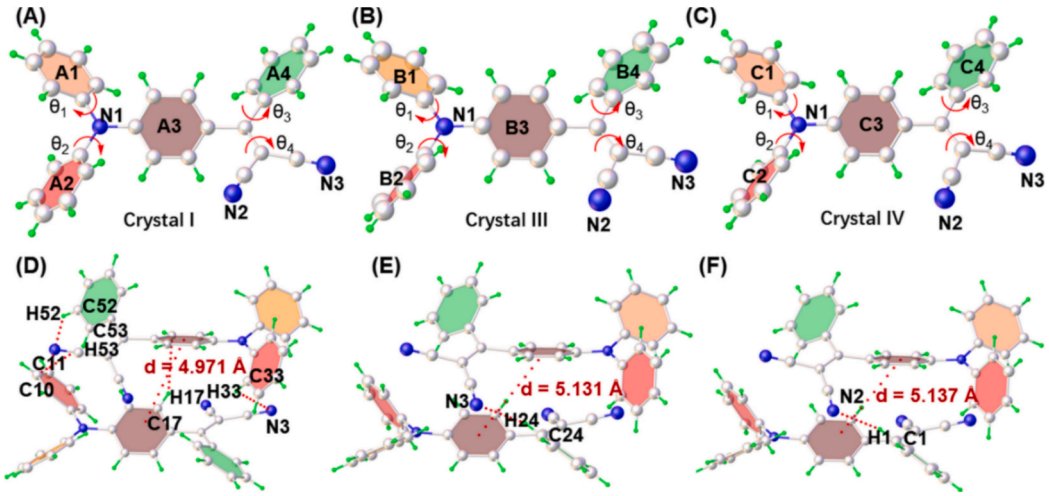

Fig. 3. Single-crystal structures and molecular conformations of **TPA-CN** polymorphs. (A–C) Crystal structures of **Crystal I, Crystal III,** and **Crystal IV** obtained by single-crystal X-ray diffraction, highlighting their twisted molecular conformations. (D-F) Crystal packing arrangements along the c-axis, showing head-to-tail stacking stabilized by multiple weak intermolecular interactions.

Table 1
Comparative torsion angle parameters (θ_1–θ_4) in **Crystals I**, **III**, and **IV.**

	θ_1 (°)	θ_2 (°)	θ_3 (°)	θ_4 (°)	d (Å)
Crystal I	60.95	59.88	57.64	60.87	4.971
Crystal II	77.27	59.89	57.24	33.13	8.022
Crystal III	56.72	78.69	57.53	67.41	5.131
Crystal IV	56.89	78.79	57.81	68.68	5.137

the order of **Crystal II** < **Crystal I** < **Crystal III** < **Crystal IV**, respectively. The centroid–centroid distances between adjacent central phenyl rings increase from 4.971 Å in **Crystal I** to 5.131 Å and 5.137 Å in **Crystals III** and IV, respectively, indicating slightly looser π-π stacking in the latter two polymorphs.

Crystals are arranged in a head-to-tail fashion, stabilized by intermolecular interactions. Notably, **Crystal I** exhibits five group C–H···π interactions (e.g., C53–H53···C12 = 2.813 Å, C50–H50···C2 = 2.820 Å) and C–H···N hydrogen bonds (C33–H33···N3 = 2.952 Å). **Crystals III** and **Crystal IV** show weaker hydrogen bonding (C24–H24···N3 = 2.885 Å in **Crystals III**, C1–H1···N2 = 2.861 Å in **Crystals IV**) and one group C–H···π interactions (Table S6). These non-covalent interactions (NCI) restrict molecular motion, suppress non-radiative decay, and enhance solid-state fluorescence quantum yield—underpinning the observed AIE. Subtle differences in weak intermolecular interactions in molecular packing across the polymorphs contribute to their distinct emission colors.

3.3. Mechanofluorochromic behavior

All four crystals exhibit bright luminescence in the solid state. **Crystal I** and **Crystal II** show red emission with λ_{emmax} at 627 nm and 603 nm, respectively. **Crystal III** displays a broad emission band (λ_{emmax} = 583 nm) with a shoulder at 643 nm, while **Crystal IV** emits at 592 nm. Fig. 4A and Table S7 present the emission spectra of **Crystals I** and **III** before and after mechanical grinding using a mortar and pestle. Both crystals exhibit pronounced blue-shifts in their photoluminescence upon grinding, indicating mechanofluorochromic (MFC) behavior. For ground **Crystal I** (**Crystal I-g**), the emission maximum shifts from 627 to 603 nm, accompanied by a notable increase in Φ_f from 46.3 % to 64.0 %. In contrast, **Crystal II** shows a decreased Φ_f of 13.3 % compared to **Crystal I**. For **Crystal III**, mechanical stimulation leads to the disappearance of a shoulder peak and a shift of the emission maximum from 583 to 579 nm, with a slight enhancement in Φ_f from 2.9 % to 3.0 %. **Crystal IV** exhibits an intermediate Φ_f of 25.1 %, higher than **Crystal III** and **Crystal III-g**. Based on the emission spectra and crystal structure parameters, the differences in emission color among the polymorphs. It is therefore speculated that **Crystal III** adopts an intermediate molecular packing arrangement between those of **Crystal I** and **Crystal IV**. Moreover, upon grinding, Crystal III may undergo a transformation into a structure resembling that of **Crystal IV**.

Time-resolved photoluminescence measurements (Fig. 4B) further support the MFC behavior. The fluorescence lifetimes are 13.51 ns (**Crystal I**), 14.78 ns (**Crystal II**), 7.14 ns (**Crystal III**), and 11.87 ns (**Crystal IV**), while the ground samples show lifetimes of 14.19 ns (**Crystal I-g**) and 6.56 ns (**Crystal III-g**), respectively. These emission shifts and lifetime changes upon grinding underscore the dynamic nature of **TPA-CN**'s aggregated-state emission and its potential in force-responsive luminescent materials. Whereas **TPA-CN** powder exhibits minimal fluorescence change upon grinding, (Fig. S9) the crystalline form demonstrates pronounced MFC behavior, indicating a molecular conformation change between distinct solid-state structures.

PXRD analysis (Fig. 4C–D) reveals that the ground samples largely retain their crystal structures, but with reduced crystallinity and slight shifts in diffraction peaks (Table S9). Specifically, the (002) diffraction plane shifts from d = 14.4187 Å (2θ = 6.123°) in **Crystal III** to 14.5016 Å (2θ = 6.090°) in **Crystal III-g**, and 14.5190 Å (2θ = 6.082°) in **Crystal IV**. These minor changes indicate preservation of unit cell parameters with reduced coherence length and potential conformational distortion.

Integrating the above-mentioned data from single X-ray crystal diffraction, PXRD and fluorescence spectra, we highlight that molecular conformation and intermolecular interactions are critical in determining the degrees of molecular motion. For example, in **Crystal I**, the presence of C–H···π interactions and hydrogen bonds enhances molecular packing and restricts molecular motion. This confinement reduces non-radiative decay pathways, resulting in a high Φ_f and a long fluorescence lifetime. In contrast, in **Crystals III/IV**, relatively weak intermolecular interactions allow greater molecular motion and vibration, leading to increased non-radiative decay, lower Φ_f, and a decreased fluorescence lifetime. Crystal densities further support these observations, with values of 1.253 g/cm^3 for **Crystal I**, 1.219 g/cm^3 for **Crystal III**, and 1.220 g/cm^3 for **Crystal IV**, respectively.

The enhanced Φ_f values observed in both **Crystal I** and **Crystal III** after grinding indicate that applied mechanical force promotes stronger intermolecular interactions and restricts intramolecular rotations, thereby increasing Φ_f and improving packing density in the aggregated state. Grinding also disrupts the long-range order of **Crystal I** and

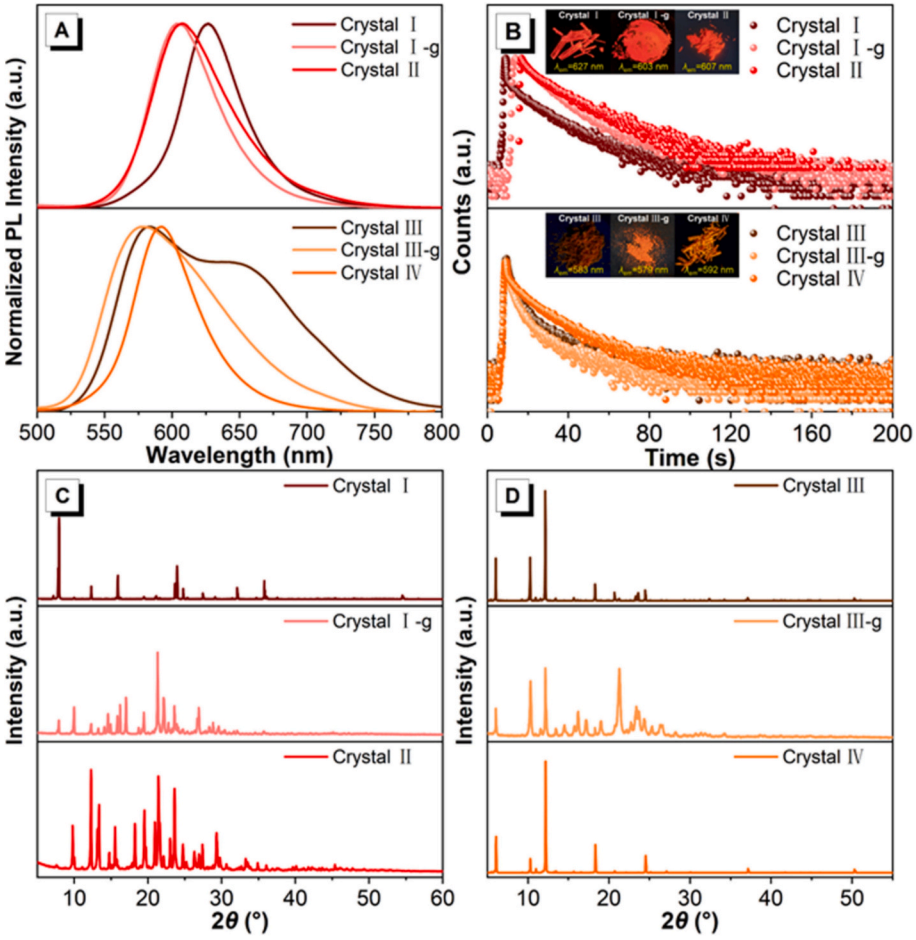

Fig. 4. Mechanochromic behavior and structural characterization of **TPA-CN** crystals. (A) Photoluminescence emission spectra of **Crystals I–IV** in the crystalline state, and ground samples of **Crystal I** and **Crystal III**, demonstrating blue-shifted emission upon mechanical grinding. (B) Time-resolved PL decay curves of **Crystals I–IV** at 298 K, indicating varied excited-state lifetimes. Inset: Fluorescence photographs of **Crystals I–IV** under UV light (λ_{ex} = 365 nm), showing distinct emission colors. (C, D) Powder X-ray diffraction patterns of the original and ground crystals. The ground samples retain the overall unit cell parameters with slight shifts in peak positions and intensity, suggesting molecular packing distortion.

Crystal III, inducing conformational changes. For **Crystal I-g**, the blue-shifted emission and enhanced Φ_f suggest that closer molecular packing is achieved through adjustments of torsion angles (θ_1–θ_4), which further restrict molecular motion and suppress non-radiative decay. In contrast, the blue-shifted emission and modest Φ_f increase observed for **Crystal III-g** are likely associated with crystal defects introduced during grinding. Collectively, these results demonstrate that the mechanochromism of **TPA-CN** is a multifaceted phenomenon governed by mechanical-force-induced modifications in molecular packing, conformational equilibrium, and supramolecular architecture, ultimately

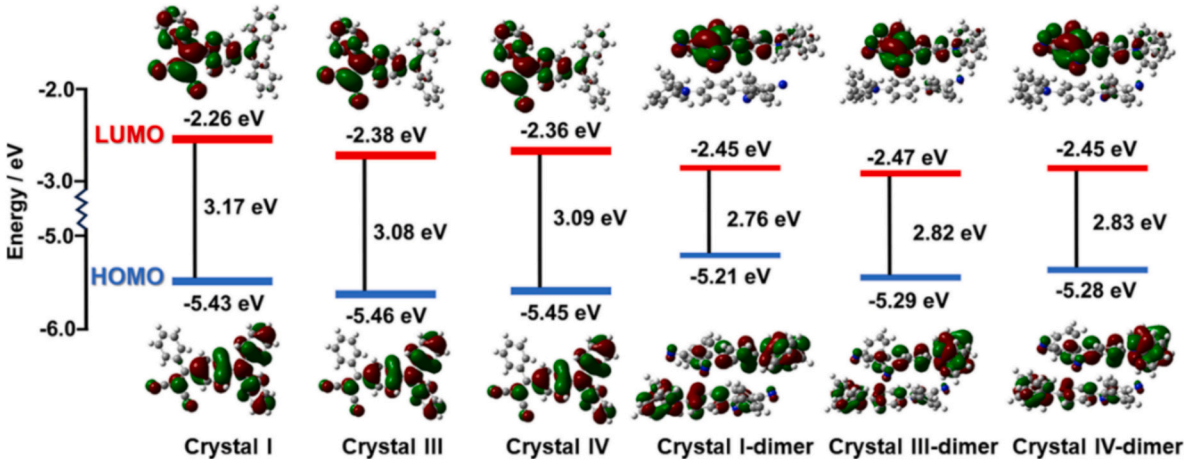

Fig. 5. Optimized molecular orbital plots of **TPA-CN** based on crystal structures of **Crystal I**, **Crystal III**, and **Crystal IV** and their corresponding crystal dimer, calculated at the B3LYP/6-31G level.

leading to tunable optical properties.

3.4. Theoretical calculation

To gain deeper insight into the electronic structure of **TPA-CN**, TD-DFT calculations were performed at the B3LYP/6-31G level using crystal-derived geometries without further optimization. As shown in Fig. 5, in the gas-phase single molecule (ground state), the HOMO is primarily localized on the diphenylamine moiety and part of the phenyl core, while the LUMO is centered on the 2-(diphenylmethylene)malononitrile unit—confirming the donor–acceptor character and revealed that changes in molecular conformation modulate the HOMO–LUMO energy levels and bandgap.

Across the three aggregated forms, the HOMO energy slightly decreases from −5.43 eV to −5.46 eV, while the LUMO energy decreases from −2.26 eV to −2.38 eV as the packing evolves from **Crystal I** to **Crystal IV** with a decreased energy gap from 3.17 eV (**Crystal I**) to 3.09 (**Crystal IV**), then to 3.08 (**Crystal III**), respectively. In the crystalline state, HOMOs are delocalized over both diphenylamine groups, while LUMOs remain confined to the acceptor unit, enhancing ICT. The calculated HOMO–LUMO gap is the smallest for **TPA-CN**-based Crystal dimer, consistent with its red-shifted emission. More interestingly, although the molecular arrangement of **TPA-CN** differs only slightly in the crystallized state, the dipole moment exhibits clear increasing trends in single-crystal molecules (**Crystal I:** 8.875 D., **Crystal III:** 9.053 D. and **Crystal IV:** 9.152 D.), but shows a remarkable decreased in the crystal dimers (**Crystal I-dimer:** 1.904 D., **Crystal III-dimer:** 1.418 D. and **Crystal IV-dimer:** 1.450 D.). These results demonstrate that solid-state intermolecular interactions and molecular conformation critically modulate electronic distribution and optical behavior, accounting for the experimentally observed mechanochromic and piezoelectric responses. [37]. Additionally, the electrochemical properties of **TPA-CN** were performed using cyclic voltammetry experiment in ACN solution. As shown in Fig. S11, compound **TPA-CN** exhibits two oxidation peaks at 0.85 V and 1.23 V, a reduction peak at 0.98 V, respectively. The HOMO and LUMO levels were evaluated by empirical equations $E_{HOMO} = -(E_{ox}^{onset} + 4.8 - E_{ox}^{onset}$ (Fc)) eV and $E_{LUMO} = E_{HOMO} + E_g$, where E_g is the energy band gap determined from the onset of the optical absorption. The calculated HOMO and LUMO energy levels is −5.18 eV and −2.73 eV, respectively, which is consistent with the **Crystal IV**-dimer sample.

The HOMOs are primarily delocalized over the diphenylamine donor units and partially on the central phenyl ring, while the LUMOs are localized on the 2-(diphenylmethylene)malononitrile acceptor moiety. These results confirm the ICT character of **TPA-CN** and reveal that changes in molecular conformation and packing subtly modulate the HOMO–LUMO energy levels and bandgap, correlating with the red- or blue-shifted emission observed in the solid state.

3.5. Hirshfield surface analysis and non-covalent interactions calculations [38,39]

To examine the influence of intermolecular interactions on emission behavior, Hirshfeld surface analysis and 2D fingerprint plots were employed to quantify non-covalent interactions in the crystalline state [40,41]. As shown in Figs. S14–S18, the red, blue, and white regions on the surfaces correspond to intermolecular interaction strengths in decreasing order. The analysis reveals that intermolecular hydrogen bonds (N—H) and C–H···π interactions dominate the crystal packing. Notably, both TPA-CN-based **Crystal III** and **Crystal IV** exhibit higher proportions of intermolecular hydrogen bonding (23.2 %) and C–H···π interactions (29.9 %) compared with **Crystal I** (21.4 % and 28.8 %, respectively). These stronger non-covalent interactions correlate with the orange-red appearance of **Crystal III** and **Crystal IV**, in contrast to the red color of **Crystal I**. Thus, subtle variations in weak intermolecular interactions likely contribute to their distinct optical appearances and emission behaviors.

Furthermore, the weak interactions of three **TPA-CN**-based crystal dimers were examined using noncovalent interaction (NCI) plots, a visual tool for assessing the strength and nature of intermolecular interactions in the crystalline state. In these plots, blue, green, and red regions correspond to strong nonbonding interactions (e.g., hydrogen bonding), weak interactions (e.g., π–π stacking and van der Waals forces), and repulsive interactions (e.g., steric effects), respectively. As shown in Fig. 6, all three dimers exhibit surfaces dominated by dispersed C–H···π interactions, although the distribution areas of these interactions vary significantly among them. Based on both Hirshfeld surface analysis and NCI calculations, it is evident that weak intermolecular interactions play a critical role in determining the crystal packing arrangements of the three **TPA-CN** crystalline systems by modulating the molecular twist angle in the solid state. This variation ultimately results in their distinct color appearances and emission behaviors.

3.6. Piezoelectric behavior

Based on crystallographic analysis and theoretical calculation, **TPA-CN**-based **Crystals I** (space group: $Pca2_1$, point group No. 29, $C2v$), **Crystals III** (space group: $P2_12_12_1$, point group No. 19, $D2$) and **Crystal IV** (space group: $P2_12_12_1$, point group No. 19, $D2$) all belong to the non-centrosymmetric point group, lacking an inversion center. This structural asymmetry endows them with intrinsic piezoelectric properties, enabling efficient conversion of mechanical stress into electric charge. However, due to the brittleness of the **Crystal III** and **Crystal IV,** there are not suitable for fabricating practical piezoelectric devices. To explore this behavior, piezoelectric devices were fabricated using **Crystal I** in a metal–organic semiconductor–metal (MOM) configuration (Fig. 7A). High-quality **TPA-CN** crystals were mounted on a polyimide substrate (thickness: 100 μm) using conductive silver paste to ensure mechanical stability and robust electrical contact.

The applied strain (ε) was estimated using the geometric relation [42]: $\varepsilon = d\sin\theta/L$, where d is the substrate thickness, θ is the angle between the tangent at the substrate end and the horizontal, and L is the horizontal distance between supports. As shown in Fig. 7B, the piezoelectric device exhibited stable current output under periodic mechanical stimulation. With increasing strain from 0.12 % to 0.51 %, the generated current rose from 52 pA to 562 pA. Notably, the output was insensitive to crystal orientation, maintaining consistent performance whether strained along the (010) or (100) axes, which are different from our previous reports (Fig. 7C, Fig. S20-S21) [21,43]. The device demonstrated excellent mechanical durability, with a minimal signal attenuation of only 8 % after 300 s of continuous operation at 0.12 % strain (Fig. 7E), highlighting its structural and functional stability.

To further validate piezoelectricity, PFM measurements were conducted on **Crystal I** mounted on a silicon wafer. Under a 3 V driving voltage, vertical surface deformation in the range of 6.42–12.8 pm was detected over a 5 μm^2 area (Fig. S22), confirming electric field-induced deformation. The piezoelectric coefficient (d_{33}) was determined from the amplitude–voltage response, yielding a value of 1.77 $pm \cdot V^{-1}$ (Fig. 7D). Although **Crystal I** exhibits a relatively low Young's modulus (6.75 GPa)—suggesting plastic deformation—it remains susceptible to brittle fracture under cyclic strain. To address this, parallel and series arrays of **TPA-CN**-based devices were fabricated to enhance both output and durability (Fig. 7F, Fig. S24-S27). Two identical **Crystal I**-based sensors (crystal 1 and crystal 2) were connected in series and in parallel. Under the same strain (0.12–0.51 %), the parallel configuration achieved a current increase from 70 to 770 pA, while the series configuration increased from 59 to 380 pA, demonstrating that parallel integration provides a more robust and amplified piezoelectric response. In addition, the parallel configuration piezoelectric devices also show a good over 80 pA (the electronic signal of parallel configuration device is higher than their single configuration devices) under 0.12 % strain, even after 300 s of continuous operation (Fig. S28). Thus, the parallel

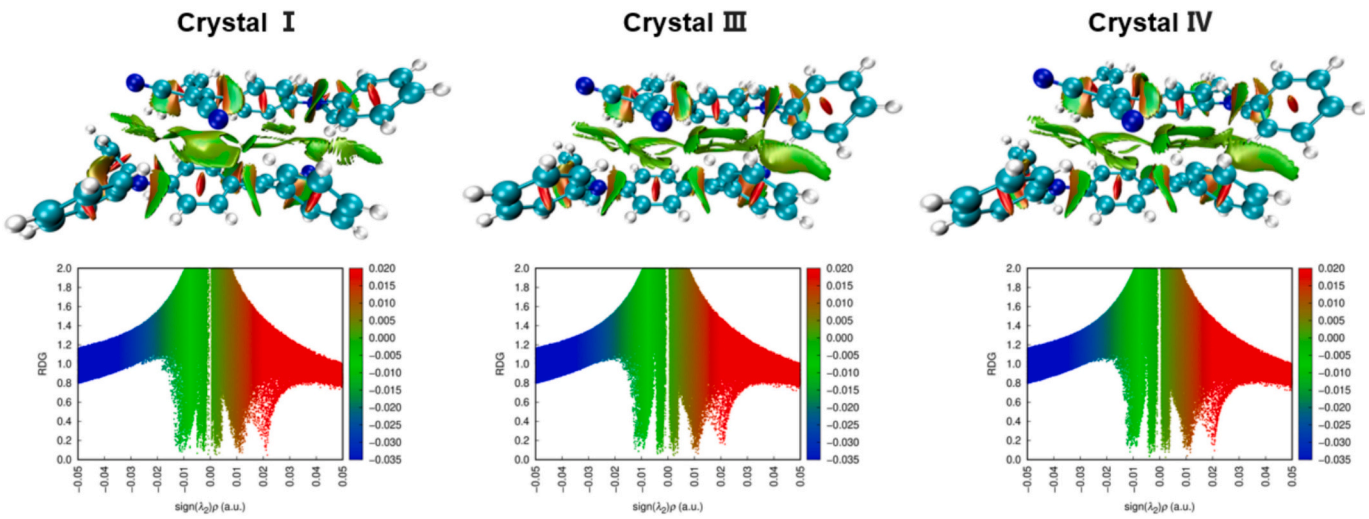

Fig. 6. NCI-index isosurfaces which characterize the interactions within the dimers of **Crystal I**, **Crystal III**, and **Crystal IV.**

configuration devices possess higher sensitivity and good stability for smart sensors.

3.7. Ground vibration detection application

Environmental micro-vibrations, often resulting from industrial (e.g., high-speed railways, heavy machinery) or natural sources (e.g., earthquakes), can compromise structural integrity, affect sensitive instruments, and disrupt daily activities [44,45]. Consequently, the development of high-sensitivity, compact piezoelectric sensors for micro-vibration detection is essential. To assess this application, a parallel-array **TPA-CN**-based sensor was used in a simulated ground vibration test (Fig. 7G). A 13.9 g steel ball was dropped from a height of 83.5 cm, impacting the ground. The impact generated a transient vibration that produced a sharp current peak of 84 pA, followed by rapid signal decay as the energy dissipated (Fig. 7H). The signal amplitude correlated with distance: as the sensor was moved from 5 cm to 40 cm away from the impact site, the peak current dropped from 84 pA to 2 pA (Fig. 7I), confirming the sensor's distance-dependent sensitivity. These results underscore the potential of the **TPA-CN**-based piezoelectric device as a highly responsive and flexible platform for low-frequency vibration detection, suitable for structural monitoring and wearable sensing applications.

3.8. Comparison and outlook

Compared to known organic piezoelectric and mechanochromic materials, **TPA-CN** offers a unique combination of excitation-tunable emission, crystal-structure-driven mechanochromism, and strain-dependent piezoelectricity (Table 2). Its d_{33} value (1.77 pm/V) is moderate but competitive among organic single crystals, and its low modulus (6.75 GPa) supports flexibility not achievable with rigid inorganic counterparts like $PbTiO_3$. Unlike many mechanochromic crystals where color changes arise from irreversible amorphization or phase transitions, **TPA-CN** retains its crystal integrity, with minor conformational distortions sufficient to induce large optical shifts. The integration of parallel device architectures further demonstrates the material's engineering compatibility and scalability for sensing platforms.

In the future, tuning the molecular dipole alignment through rational substituent engineering or supramolecular templating may enhance piezoelectricity further. Incorporation into hybrid films or elastomeric matrices could extend the functionality to wearable and implantable devices. Finally, coupling this AIEgen framework with ferroelectric or triboelectric systems could enable synergistic multimodal sensors or self-powered optoelectronic platforms. This study lays the foundation for a new generation of polymorphic, multifunctional materials that bridge molecular design and macroscopic device performance.

4. Conclusion

In summary, this study presents a comprehensive investigation into the motion–structure–property relationship of a malononitrile-based AIEgen, **TPA-CN**. Through systematic analysis of its molecular dynamics, crystal structures, mechanochromic behavior, and piezoelectric properties, we elucidate how subtle intramolecular motions and packing variations give rise to distinct macroscopic functionalities. In solution, **TPA-CN** exhibits excitation-dependent emission due to multiple excited states, allowing color tuning from sky-blue to white and red. In the crystalline state, small conformational changes and intermolecular packing rearrangements lead to mechanochromic luminescence shifts (blue-shifted by 9–20 nm), without undergoing crystal phase transitions, as confirmed by SXRD and PXRD.

Notably, **Crystal I**, crystallizing in the non-centrosymmetric space group $Pca2_1$, exhibits excellent strain-dependent piezoelectric performance, with current outputs increasing from 52 pA to 562 pA under strains ranging from 0.12 % to 0.51 %, alongside a Young's modulus of 6.75 GPa and d_{33} value of 1.77 pm·V^{-1}. Furthermore, parallel device configurations effectively amplified signal strength and enabled the sensitive detection of ground vibrations, demonstrating practical applicability in low-frequency mechanical sensing. This work provides new insight into the interplay between molecular motion, crystal packing, and functional properties in AIEgens. It establishes **TPA-CN** as a multifunctional platform for applications in flexible electronics, mechanosensors, and piezoelectric devices, bridging the gap between molecular-level design and macroscopic functionality in advanced smart materials.

CRediT authorship contribution statement

Kaiwei Huang: Investigation, Data curation. **Tao Jiang:** Investigation, Formal analysis. **Jiexi Liang:** Investigation. **Xiaoxue Chen:** Visualization. **Wei Liu:** Data curation. **Wenxuan Cai:** Visualization. **Chongyang Zeng:** Data curation. **Junru Chen:** Writing – review & editing. **Jun Zhang:** Software, Data curation. **Changyong (Chase) Cao:** Writing – review & editing, Resources, Methodology. **Xing Feng:** Writing – original draft, Supervision, Project administration.

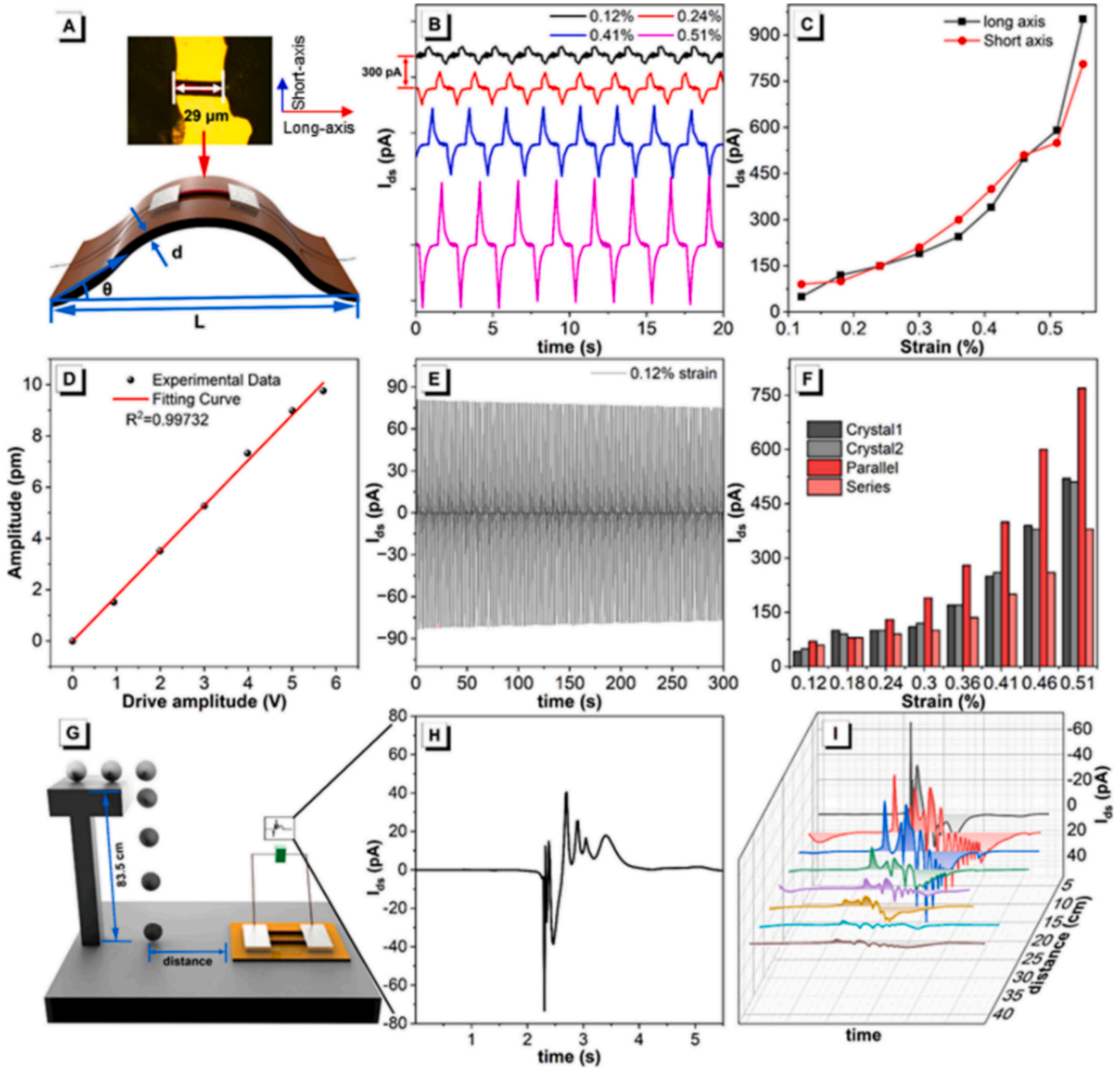

Fig. 7. Piezoelectric and vibration sensing performance of **TPA-CN**-based **Crystal I**. (A) Schematic and optical microscope image of the fabricated piezoelectric device with MOM configuration. (B) Output current of **Crystal I**-based devices under increasing strain (0.12–0.51 %) along the (010) axis. (C) Comparison of current output along (010) and (100) axes showing orientation-independent piezoelectric response. (D) PFM measurement showing vertical displacement under a 3 V driving voltage and calculated piezoelectric coefficient (d_{33} = 1.77 pm·V^{-1}). (E) Current output stability under continuous operation for 300 s at 0.12 % strain. (F) Output current comparison for single, series, and parallel configurations of **Crystal I**-based devices under various strains. (G) Schematic of ground vibration simulation using a free-falling steel ball. (H) Transient current response upon ground impact. (I) Distance-dependent current output from 5 to 40 cm, illustrating high sensitivity and attenuation with distance.

Table 2
Comparison of the new AIEgen and reported piezoelectric materials.

Material	d_{33} (pm V^{-1})	Young's modulus (GPa)	Emission tunability	Mechanochromism	Crystal symmetry
TPA-CN (this work)	1.77	6.75	Blue–Red (λ_{ex}-dependent)	Yes	*Pca*2$_1$ (non-centrosymmetric)
π–π stacked pyrene crystal [16]	8.02	9.0	None	Yes	*P*2$_1$ (polar)
Co(II) coordination cage [15]	2.8	12.5	None	No	*C*2 (non-centrosymmetric)
PVDF (reference organic piezoelectric)	−10.0	−1.0	None	No	β-phase (polar)
$PbTiO_3$ (inorganic benchmark)	−300.0	63.0	None	No	Tetragonal

Declaration of competing interest

The authors declare that they have no known competing financial interests or personal relationships that could have appeared to influence the work reported in this paper.

Acknowledgements

This work was supported by the National Natural Science Foundation of China (21975054). XF thanks Dr. Kai Yan (Analysis and Test Center, Guangdong University of Technology) for structure characterization. CC acknowledges the support from Case Western Reserve University.

Appendix A. Supplementary data

Supplementary data to this article can be found online at https://doi.org/10.1016/j.cej.2025.168741.

Data availability

Data will be made available on request.

References

[1] Y. Tu, Z. Zhao, J.W.Y. Lam, B.Z. Tang, Aggregate science: much to explore in the meso world, Matter 4 (2) (2021) 338–349.
[2] H. Zhang, Z. Zhao, A.T. Turley, L. Wang, P.R. McGonigal, Y. Tu, Y. Li, Z. Wang, R.T. K. Kwok, J.W.Y. Lam, B.Z. Tang, Aggregate science: from structures to properties, Adv. Mater. 32 (36) (2020) 2001457.
[3] J. Mei, N.L.C. Leung, R.T.K. Kwok, J.W.Y. Lam, B.Z. Tang, Aggregation-induced emission: together we shine, united we soar!, Chem. Rev. 115 (21) (2015) 11718–11940.
[4] Z. Ding, B. Wu, Z. Liu, H. Wang, F. Gao, X. Wei, Z. Zhao, P. Alam, Z. Qiu, B.Z. Tang, Harnessing photocycloreversion for dimer construction and photoactivation: from molecule to aggregate, Aggregate n/a (n/a) (2025) e70024.
[5] G. Chakraborty, J.N. Malegaonkar, S.V. Bhosale, P.K. Singh, H. Pal, Host-assisted aggregation-induced emission of a tetraphenylethylene derivative and its responses toward external stimuli, J. Phys. Chem. B 125 (40) (2021) 11122–11133.
[6] P. Chowdhury, A. Banerjee, B. Saha, K. Bauri, P. De, Stimuli-responsive aggregation-induced emission (AIE)-active polymers for biomedical applications, ACS Biomater Sci. Eng. 8 (10) (2022) 4207–4229.
[7] Y. Huang, L. Ning, X. Zhang, Q. Zhou, Q. Gong, Q. Zhang, Stimuli-fluorochromic smart organic materials, Chem. Soc. Rev. 53 (3) (2024) 1090–1166.
[8] Y. Guo, A. Wu, Q. Zhang, M. Zhao, Y. Gong, S. Liu, M. Khan, H. Song, J. Yoon, Q. Hu, Mechanochromic luminescent material with high quantum yield for multi-mode anti-counterfeiting applications, Chem. Eng. J. 497 (2024) 154721.
[9] M. Chakraborty, M. Chakravarty, Varied optical features and mechanofluorochromism in dicyanovinyl- vs. cyanoacrylicacid-linked twisted π-conjugates: a potential reusable platform for security applications, Mater. Today Chem. 35 (2024) 101836.
[10] Y.-X. Peng, H.-Q. Liu, W. Huang, T. Tao, Isomeric pair of E/Z tetraphenylethene-cored Luminogens showing distinguishing Mechanoresponsive luminescence turn-on and two-color behavior, J. Phys. Chem. C 126 (14) (2022) 6491–6498.
[11] X. Li, Z. Zhu, Y. Lyu, C. Zhang, S. Hu, Q. Wang, W.-H. Zhu, Application of AIEgens in temperature detection, ACS Mater. Lett. 6 (4) (2024) 1356–1370.
[12] S. Bhunia, S.K. Karan, R. Chowdhury, I. Ghosh, S. Saha, K. Das, A. Mondal, A. Nanda, B.B. Khatua, C.M. Reddy, Mechanically flexible piezoelectric organic single crystals for electrical energy harvesting, Chem 10 (6) (2024) 1741–1754.
[13] B. Prusti, P. Sarkar, S.K. Pati, M. Chakravarty, Multistimuli and fingertip-triggered luminescence switching: a five-colored ink-free rewritable secured platform with strongest red emission, J. Mater. Chem. C 9 (30) (2021) 9555–9570.
[14] B. Prusti, S. Tripathi, P. Sivasakthi, P.K. Samanta, M. Chakravarty, Tuning solid-state emissions via twists and turns in polymorphic self- and cross-coupled dianthrylethenes, Adv Opt Mater n/a(n/a) (2025) e00985.
[15] D. Tu, J. Zhang, Y. Zhang, H.H.Y. Sung, L. Liu, R.T.K. Kwok, J.W.Y. Lam, I. D. Williams, H. Yan, B.Z. Tang, How do molecular motions affect structures and properties at molecule and aggregate levels? J. Am. Chem. Soc. 143 (30) (2021) 11820–11827.
[16] J.C.P. Curie, Développement par compression de l'électricité polaire dans les cristaux hémièdres à faces inclinées, Bull. Mineral. 3 (4) (1880) 90–93.
[17] R. Wang, J. Sui, X. Wang, Natural piezoelectric biomaterials: a biocompatible and sustainable building block for biomedical devices, ACS Nano 16 (11) (2022) 17708–17728.
[18] R. Haldar, A. Kumar, B. Mallick, S. Ganguly, D. Mandal, M. Shanmugam, Discrete molecular copper(II) complex for efficient piezoelectric energy harvesting above room-temperature, Angew. Chem. Int. Ed. 62 (9) (2023) e202216680.
[19] J. Wei, G. Zhang, S. Xie, Z. Zhang, T. Gao, M. Zhang, X. Li, Enhanced interfacial electric field of an S-scheme heterojunction by an ultrasonication-triggered piezoelectric effect for sonocatalytic therapy of bacterial infections, Angew. Chem. Int. Ed. 64 (16) (2025) e202500441.
[20] N. Prajesh, V. Kushwaha, D.R. Naphade, B. Praveenkumar, J.K. Zaręba, T. D. Anthopoulos, R. Boomishankar, Flexible piezoelectric nanogenerator with a ferroelectric metal–ligand cage for self-powered sensor applications, ACS Appl Energy Mater 8 (7) (2025) 4648–4655.
[21] X. Song, X. Wang, W. Liu, X. Chen, S. Li, M.S. Islam, L. Li, X. Zhao, C. Redshaw, Y. Zhao, C. Cao, X. Feng, Organic photo-responsive piezoelectric materials based on pyrene molecules for flexible sensors, Adv. Electron. Mater. n/a (n/a) (2025) 2400933.
[22] X. Jiang, J. Kim, K. Kim, Relaxor-PT single crystal piezoelectric sensors, Crystals (2014) 351–376.
[23] S. Yagai, T. Seki, H. Aonuma, K. Kawaguchi, T. Karatsu, T. Okura, A. Sakon, H. Uekusa, H. Ito, Mechanochromic luminescence based on crystal-to-crystal transformation mediated by a transient amorphous state, Chem. Mater. 28 (1) (2016) 234–241.
[24] D. Yang, S. Ye, J. Ge, From metastable colloidal crystalline arrays to fast responsive mechanochromic photonic gels: an organic gel for deformation-based display panels, Adv. Funct. Mater. 24 (21) (2014) 3197–3205.
[25] S. Ito, S. Wakiyama, H. Chen, M. Abekura, H. Uekusa, R. Ikemura, Y. Imai, Contrasting mechanochromic luminescence of enantiopure and racemic pyrenylprolinamides: elucidating solid-state excimer orientation by circularly polarized luminescence, Angew. Chem. Int. Ed. 64 (11) (2025) e202422913.
[26] J.-H. Hu, R.-X. Hou, C. Liu, Y.-P. Wang, Y.-F. Liu, Y. Huang, Z. Tao, X. Xiao, Ultra-long room temperature phosphorescent materials based on tetraphenylethylene derivatives for anti-counterfeiting and encryption applications, Chem. Eng. J. 491 (2024) 152177.
[27] Y. Xie, Y. Zheng, X. Bai, Y. Tang, S. Zhao, C. Guo, Z. Ma, Y. Shi, X. Mao, H. Liang, Q. Wan, Recent process of NIR-type AIE-active fluorescent materials for biomedical applications of fluorescent imaging and phototherapeutics, Chem. Eng. J. 507 (2025) 160692.
[28] J. Wang, Y. Wang, Z. Li, C. Xie, M. Khan, X. Peng, F. Yu, Triphenylamine-AIEgens photoactive materials for cancer theranostics, Chin. Chem. Lett. 35 (6) (2024) 108934.
[29] R. Qu, X. Zhen, X. Jiang, Emerging designs of aggregation-induced emission agents for enhanced phototherapy applications, CCS Chemistry 4 (2) (2021) 401–419.
[30] G. Yang, W.-X. Zhao, L. Liang, Z.-M. Xue, F. Meng, Y.-Q. Kong, H.-T. Lin, S.-H. Chen, C.-Z. Wang, Tunable containing malononitrile AIEgens with reversible mechanochromic behaviors and promising applications, Chem. Eng. J. 515 (2025) 163597.
[31] M. Bruker, APEX2 and SAINT, Bruker AXS Inc., Wisconsin, USA, 2016.
[32] G. Sheldrick, SHELXT - integrated space-group and crystal-structure determination, Acta Crystallogr. A 71 (1) (2015) 3–8.
[33] G. Sheldrick, Crystal structure refinement with SHELXL, Acta Crystallogr. C 71 (1) (2015) 3–8.
[34] L. Zhan, Z. Chen, S. Gong, Y. Xiang, F. Ni, X. Zeng, G. Xie, C. Yang, A simple organic molecule realizing simultaneous TADF, RTP, AIE, and mechanoluminescence: understanding the mechanism behind the multifunctional emitter, Angew. Chem. Int. Ed. 58 (49) (2019) 17651–17655.
[35] N.K. M, D.L. Lyngkhoi, S. Gaikwad, J. Samanta, R. Ahamed, S. Khatua, S. Pramanik, Excitation wavelength-dependent multi-coloured and white-light emissive pyrene-based hydrazones: suppression of Kasha's rule, Chem. Commun. 59 (95) (2023) 14122–14125.
[36] X. Feng, J. Zhang, Z. Hu, Q. Wang, M.M. Islam, J.-S. Ni, M.R.J. Elsegood, J.W. Y. Lam, E. Zhou, B.Z. Tang, Pyrene-based aggregation-induced emission luminogens (AIEgen): structure correlated with particle size distribution and mechanochromism, J. Mater. Chem. C 7 (23) (2019) 6932–6940.
[37] D. Qiao, J.-Y. Wang, L.-Y. Zhang, F.-R. Dai, Z.-N. Chen, Aggregation-induced emission enhancement and reversible mechanochromic luminescence of quinoline-based zinc(ii)–Schiff base complexes, Dalton Trans. 48 (29) (2019) 11045–11051.
[38] T. Lu, F. Chen, Multiwfn: A multifunctional wavefunction analyzer, J. Comput. Chem. 33 (5) (2012) 580–592.
[39] T. Lu, A comprehensive electron wavefunction analysis toolbox for chemists, Multiwfn, J. Chem. Phys. 161 (8) (2024) 082503.
[40] M.J. Turner, S.P. Thomas, M.W. Shi, D. Jayatilaka, M.A. Spackman, Energy frameworks: insights into interaction anisotropy and the mechanical properties of molecular crystals, Chem. Commun. 51 (18) (2015) 3735–3738.
[41] B. Prusti, S. Tripathi, P. Sivasakthi, P.K. Samanta, M. Chakravarty, Solution and solid-state emissive organophosphonates with high-contrast reversible mechanofluorochromism: beyond the classical frameworks, ACS Appl Opt Mater 1 (4) (2023) 889–897.
[42] J.-N. Kim, J. Lee, T.W. Go, A. Rajabi-Abhari, M. Mahato, J.Y. Park, H. Lee, I.-K. Oh, Skin-attachable and biofriendly chitosan-diatom triboelectric nanogenerator, Nano Energy 75 (2020) 104904.
[43] L. Li, J. Zhang, C. Yang, L. Huang, J. Zhang, J. Bai, C. Redshaw, X. Feng, C. Cao, N. Huo, J. Li, B.Z. Tang, Stimuli-responsive materials from ferrocene-based organic small molecule for wearable sensors, Small 17 (46) (2021) 2103125.
[44] Z. Wang, A. Tang, D. Huang, C. Wu, Z. Huang, A novel environmental vibration analysis system and its application in isolation of environmental vibration induced by high-speed train in Harbin frozen soil site, Appl. Acoust. 193 (2022) 108781.
[45] J. Wang, X. Xiao, L. Peng, J. Wang, Y. He, X. Sheng, Modelling metro-induced environmental vibration by combining physical-numerical and deep learning methods, Mech. Syst. Signal Process. 220 (2024) 111687.